

Large Eddy Simulation of Surging Airfoils at High Advance Ratio and Reynolds Number

Jitesh Rane* and Onkar Sahni†
Rensselaer Polytechnic Institute, Troy, NY 12180, USA

Large eddy simulation (LES) is performed for a surging NACA 0012 airfoil at high advance ratios and Reynolds numbers. The airfoil is subjected to sinusoidal oscillations in the streamwise direction at a fixed frequency and angle of attack in a constant free-stream flow. Three Reynolds numbers of $Re=40,000$, $200,000$ and $1,000,000$ are considered together with two advance ratios of $\lambda=1.0$ and 1.2 , i.e., six cases are considered in total. We note that at the higher advance ratio the relative flow velocity becomes negative and a reversed flow condition is reached.

Overall a similar trend is observed in the lift force among all cases. The peak normalized lift is about 9% lower for the highest Reynolds number case as compared to the lower Reynolds number cases for each advance ratio. On the other hand, the peak normalized lift is about 21% higher for the higher advance ratio case as compared to the lower advance ratio case for each Reynolds number, which is the difference in the peak dynamic pressure between the two advance ratios. Flow field also reveals a similar behavior among all cases with prominent features of flow separation near the (geometric) leading edge during the beginning of the retreating phase and formation of a dominant leading edge vortex (LEV). We observe that as the Reynolds number increases the LEV is formed later in the cycle (for a given advance ratio) while as the advance ratio increases it is formed earlier in the cycle (for a given Reynolds number). LEV evolution is also quantified based on its size and position. The central core of the LEV is found to fit the Rankine vortex model. As expected, a larger LEV is obtained for the lowest Reynolds number while LEV remains closest to the airfoil for the highest Reynolds number. At the higher advance ratio the LEV initially moves to the left past the geometric leading edge for each Reynolds number. This is expected since the relative flow velocity becomes negative (or a reversed flow condition is obtained). Further, the slope of the horizontal displacement in each case is remarkably close to the free-stream velocity, i.e., the LEV is advected in the horizontal direction at the free-stream velocity.

I. Introduction

Surging motion arises in many aerodynamic problems. For example, in a forward flight for a rotorcraft. In a forward flight, rotor blades are subjected to fluctuating local velocity due to the forward motion of the rotorcraft and rotational motion of the blade along the azimuth. In a high-speed forward flight or at a high advance ratio (i.e., the ratio of forward to rotational motion), the relative velocity can reverse in direction near the inboard portion of the retreating blade. The oscillatory relative velocity causes large changes in the lift force, with high lift generated as the blade advances and small to no lift generated as the blade retreats. Analytical models have been formulated in an attempt to predict this behavior, but often pose issues when there is complete flow reversal and the sharp trailing edge temporarily acts as the aerodynamic leading edge. Studying a rotor blade under a reversed flow condition is necessary to improve the forward flight capabilities of a rotorcraft. One way to achieve this is to employ high-fidelity simulations with reliable modeling.

Some of the recent work to understand these flow phenomena has been done by conducting experiments in a quasi-3D environment by subjecting a blade model to cyclic surging and/or pitching motions. Greenblatt *et al.* [1] looked into the effects of fluctuating free-stream velocity and cyclic pitching on an airfoil section through experiments. Granlund *et al.* [2] considered the effect of large streamwise oscillations including a reverse flow regime, for different reduced frequencies, through water tunnel experiments. Numerical simulations have also been used as an effective way to further understand these effects. Numerical investigations on a quasi-3D model include that of Visbal [3] and Gross and Wen [4], with a high-order finite difference based large eddy simulation (LES), and Strangfeld [5], with unsteady

*Graduate Student, Department of Mechanical, Aerospace and Nuclear Engineering, AIAA Student Member

†Associate Professor, Department of Mechanical, Aerospace and Nuclear Engineering, AIAA Senior Member

Reynolds-averaged Navier-Stokes (URANS) simulations. Hodara *et al.* [6] investigated a pitching airfoil in a constant reverse flow (leading to a reserve dynamic stall) through a joint wind tunnel testing and numerical simulation based on a hybrid RANS-LES approach. Others have chosen to study the entire rotor in a forward flight using experimental testing [7] or a RANS or hybrid RANS-LES approach, e.g., see [8, 9].

In this study, large eddy simulation (LES) is used to predict flow over an oscillating airfoil. Current LES uses a combined subgrid-scale model which uses the residual-based variational multiscale (RBVMS) model along with the dynamic Smagorinsky model [10]. An arbitrary Lagrangian Eulerian (ALE) description is used to account for the relative motion of the airfoil [11].

Three Reynolds numbers of $Re=40,000$, $200,000$ and $1,000,000$ are considered together with two advance ratios of $\lambda=1.0$ and 1.2 , i.e., six cases are considered in total. We note that at the higher advance ratio the relative flow velocity becomes negative and a reversed flow condition is reached. LES predictions for the force response, flow field and leading edge vortex (LEV) evolution are presented for all six cases.

The organization of this paper is as follows. The combined model formulation and dynamic procedure used in LES are discussed in Sections II.A and II.B (within Section II), respectively. The numerical setup is described in Section III. Results are presented in Section IV. Section IV.A presents the lift force data, Section IV.B examines the flow field and Section IV.C presents the LEV evolution. Concluding remarks are provided in Section V.

II. Dynamic Large Eddy Simulations

A. Combined Model Formulation

This work uses the incompressible Navier Stokes equations in the arbitrary Lagrangian Eulerian (ALE) description. The strong form of the equations is given as

$$\begin{aligned} u_{k,k} &= 0 \\ u_{i,t} + (u_j - u_j^m)u_{i,j} &= -p_{,i} + \tau_{ij,y}^y + f_i \end{aligned} \quad (1)$$

where u_i is the velocity vector, u_i^m is the mesh velocity vector, p is the pressure (scaled by the constant density), $\tau_{ij}^y = 2\nu S_{ij}$ is the symmetric (Newtonian) viscous stress tensor (scaled by the density), ν is the kinematic viscosity, $S_{ij} = 0.5(u_{i,j} + u_{j,i})$ is the strain-rate tensor, and f_i is the body force vector (per unit mass). Note that Einstein summation notation is used.

The weak form is stated as follows: find $\mathbf{u} \in \mathcal{S}$ and $p \in \mathcal{P}$ such that

$$\begin{aligned} B(\{w_i, q\}, \{u_i, p\}; u_i^m) &= \int_{\Omega} [w_i(u_{i,t} + u_i u_{j,j}^m) + w_{i,j}(-u_i(u_j - u_j^m) + \tau_{ij}^y - p\delta_{ij}) - q_k u_k] d\Omega \\ &+ \int_{\Gamma_h} [w_i(u_i(u_j - u_j^m) - \tau_{ij}^y + p\delta_{ij})n_j + q u_k n_k] d\Gamma_h \\ &= \int_{\Omega} w_i f_i d\Omega \end{aligned} \quad (2)$$

for all $\mathbf{w} \in \mathcal{W}$ and $q \in \mathcal{P}$. \mathcal{S} and \mathcal{P} are suitable trial/solution spaces and \mathcal{W} is the test/weight space. \mathbf{w} and q are the weight functions for the velocity and pressure variables, respectively. Ω is the spatial domain and Γ_h is the portion of the domain boundary with Neumann or natural boundary conditions.

The above weak form can be written concisely as: find $\mathbf{U} \in \mathcal{U}$ such that

$$B(\mathcal{W}, \mathbf{U}; u_i^m) = (\mathcal{W}, \mathbf{F}) \quad (3)$$

for all $\mathcal{W} = [\mathbf{w}, q]^T \in \mathcal{V}$. $\mathbf{U} = [\mathbf{u}, p]^T$ is the vector of unknown solution variables and $\mathbf{F} = [\mathbf{f}, 0]^T$ is the source vector. The solution and weight spaces are: $\mathcal{U} = \{\mathbf{U} = [\mathbf{u}, q]^T | \mathbf{u} \in \mathcal{S}; p \in \mathcal{P}\}$ and $\mathcal{V} = \{\mathcal{W} = [\mathbf{w}, q]^T | \mathbf{w} \in \mathcal{W}; q \in \mathcal{P}\}$, respectively.

Throughout this text $B(\cdot, \cdot)$ is used to represent the semi-linear form that is linear in its first argument and (\cdot, \cdot) is used to denote the L_2 inner product. $B(\mathcal{W}, \mathbf{U}; u_i^m)$ is split into bilinear and semi-linear terms as shown below.

$$B(\mathbf{W}, \mathbf{U}; u_l^m) = B_1(\mathbf{W}, \mathbf{U}; u_l^m) + B_2(\mathbf{W}, \mathbf{U}) = (\mathbf{W}, \mathbf{F}) \quad (4)$$

where $B_1(\mathbf{W}, \mathbf{U}; u_l^m)$ contains the bilinear terms and $B_2(\mathbf{W}, \mathbf{U})$ consists of the semi-linear terms. These are defined as

$$\begin{aligned} B_1(\mathbf{W}, \mathbf{U}; u_l^m) &= \int_{\Omega} [w_i(u_{i,t} + u_i u_{j,j}^m) + w_{i,j}(u_i u_j^m + \tau_{ij}^v - p \delta_{ij}) - q_k u_k] d\Omega \\ &+ \int_{\Gamma_h} [w_i(-u_i u_j^m - \tau_{ij}^v + p \delta_{ij}) n_j + q u_k n_k] d\Gamma_h \end{aligned} \quad (5)$$

$$B_2(\mathbf{W}, \mathbf{U}) = - \int_{\Omega} w_{i,j} u_i u_j d\Omega + \int_{\Gamma_h} w_i u_i u_j n_j d\Gamma_h \quad (6)$$

The Galerkin weak form is obtained by considering the finite-dimensional or discrete solution spaces $\mathcal{S}^h \subset \mathcal{S}$ and $\mathcal{P}^h \subset \mathcal{P}$ and the weight space $\mathcal{W}^h \subset \mathcal{W}$, where the superscript h is used as a mesh parameter to denote discretized spaces and variables in a finite element context. Using these spaces, $\mathcal{U}^h = \{\mathbf{U}^h = [\mathbf{u}^h, p^h]^T \mid \mathbf{u}^h \in \mathcal{S}^h; p^h \in \mathcal{P}^h\}$ and $\mathcal{V}^h = \{\mathbf{W}^h = [\mathbf{w}^h, q^h]^T \mid \mathbf{w}^h \in \mathcal{W}^h; q^h \in \mathcal{P}^h\}$ are defined. The Galerkin weak form is then stated concisely as: find $\mathbf{U}^h \in \mathcal{U}^h$ such that

$$B(\mathbf{W}^h, \mathbf{U}^h) = (\mathbf{W}^h, \mathbf{F}) \quad (7)$$

for all $\mathbf{W}^h \in \mathcal{V}^h$. Note for brevity we have dropped u_l^m term in the arguments of the semi-linear form. The Galerkin weak formulation corresponds to a method for direct numerical simulation since no modeling is employed. However, when the finite-dimensional spaces are incapable of representing the fine/small scales, the Galerkin formulation yields an inaccurate solution. A model term is added to overcome this difficulty, e.g., as done in the residual-based variational multiscale (RBVMS) formulation.

In RBVMS, a set of model terms is added to the Galerkin weak form that results in the following variational formulation: find $\mathbf{U}^h \in \mathcal{U}^h$ such that

$$B(\mathbf{W}^h, \mathbf{U}^h) + M_{rbvms}(\mathbf{W}^h, \mathbf{U}^h) = (\mathbf{W}^h, \mathbf{F}) \quad (8)$$

for all $\mathbf{W}^h \in \mathcal{V}^h$. M_{rbvms} represents the set of model terms due to the RBVMS approach.

A scale separation is used to decompose the solution and weight spaces as $\mathcal{S} = \mathcal{S}^h \oplus \mathcal{S}'$ and $\mathcal{P} = \mathcal{P}^h \oplus \mathcal{P}'$, and $\mathcal{W} = \mathcal{W}^h \oplus \mathcal{W}'$, respectively. Thus, the solution and weight functions are decomposed as $u_i = u_i^h + u_i'$ and $p = p^h + p'$ or $\mathbf{U} = \mathbf{U}^h + \mathbf{U}'$, and $w_i = w_i^h + w_i'$ and $q = q^h + q'$ or $\mathbf{W} = \mathbf{W}^h + \mathbf{W}'$, respectively. Note that coarse-scale or resolved quantities are denoted by $(\cdot)^h$ and fine-scale or unresolved quantities by $(\cdot)'$. The coarse-scale quantities are resolved by the grid whereas the effects of the fine scales on the coarse scales are modeled. In RBVMS, the fine scales are modeled as a function of the strong-form residual due to the coarse-scale solution. This is represented abstractly as $\mathbf{U}' = \mathcal{F}(\mathbf{R}(\mathbf{U}^h); \mathbf{U}^h)$, where $\mathbf{R}(\cdot) = [\mathbf{R}^m(\cdot), \mathbf{R}^c(\cdot)]^T$ is the strong-form residual of the equations with $\mathbf{R}^m(\cdot)$ (or $\mathbf{R}_i^m(\cdot)$) and $\mathbf{R}^c(\cdot)$ as those of the momentum and continuity equations, respectively. Specifically, the fine-scale quantities are modeled as $u_i' \approx -\tau_M \mathbf{R}_i^m(u_k^h, p^h; u_l^m)$ and $p' \approx -\tau_C \mathbf{R}^c(u_k^h)$, where τ_C and τ_M are stabilization parameters (e.g., see details in Tran and Sahni [10]). This provides a closure to the coarse-scale problem as it involves coarse-scale solution as the only unknown. This is why $M_{rbvms}(\mathbf{W}^h, \mathbf{U}^h)$ is written only in terms of the unknown coarse-scale solution \mathbf{U}^h . In summary, $M_{rbvms}(\mathbf{W}^h, \mathbf{U}^h)$ can be written as

$$\begin{aligned}
M_{rbvms}(\mathbf{W}^h, \mathbf{U}^h) = & \\
\sum_e \int_{\Omega_e^h} [& \underbrace{-(w_i^h u_{j,j}^m + w_{i,j}^h u_j^m) \tau_M R_i^m(u_k^h, p^h; u_l^m)}_{M_{rbvms}^{ALE}(\mathbf{W}^h, \mathbf{U}^h)} \\
& + \underbrace{q_{,i}^h \tau_M R_i^m(u_k^h, p^h; u_l^m)}_{M_{rbvms}^{cont}(\mathbf{W}^h, \mathbf{U}^h)} + \underbrace{w_{i,j}^h \tau_C R^c(u_k^h) \delta_{ij}}_{M_{rbvms}^P(\mathbf{W}^h, \mathbf{U}^h)} \\
& + \underbrace{w_{i,j}^h (u_i^h \tau_M R_j^m(u_k^h, p^h; u_l^m) + \tau_M R_i^m(u_k^h, p^h; u_l^m) u_j^h)}_{M_{rbvms}^C(\mathbf{W}^h, \mathbf{U}^h)} \\
& \left. - \underbrace{w_{i,j}^h \tau_M R_i^m(u_k^h, p^h; u_l^m) \tau_M R_j^m(u_k^h, p^h)}_{M_{rbvms}^R(\mathbf{W}^h, \mathbf{U}^h)} \right] d\Omega_e^h
\end{aligned} \tag{9}$$

Note that all model terms are written in terms of the resolved scales within each element (where e denotes an element and contributions from all elements are summed). The last model term is used to represent the Reynolds stresses (i.e., M_{rbvms}^R) while the two terms prior to it are used to represent the cross-stress terms (i.e., M_{rbvms}^C).

In previous studies [10, 12], it was found that the RBVMS model provides a good approximation for the turbulent dissipation due to the cross stresses but the dissipation due to the Reynolds stresses is underpredicted and turns out to be insufficient. Therefore, a combined subgrid-scale model was employed which uses the RBVMS model for the cross-stress terms and the dynamic Smagorinsky eddy-viscosity model for the Reynolds stress terms. This was done in both a finite element code [10, 13] and a spectral code [12]. The combined subgrid-scale model is defined as

$$B(\mathbf{W}^h, \mathbf{U}^h) + M_{comb}(\mathbf{W}^h, \mathbf{U}^h; C_S, h) = (\mathbf{W}^h, \mathbf{F}) \tag{10}$$

where the combined model term is as follows

$$\begin{aligned}
M_{comb}(\mathbf{W}^h, \mathbf{U}^h; C_S, h) = & M_{rbvms}^{ALE}(\mathbf{W}^h, \mathbf{U}^h) + M_{rbvms}^{cont}(\mathbf{W}^h, \mathbf{U}^h) \\
& + M_{rbvms}^P(\mathbf{W}^h, \mathbf{U}^h) + M_{rbvms}^C(\mathbf{W}^h, \mathbf{U}^h) \\
& + (1 - \gamma) M_{rbvms}^R(\mathbf{W}^h, \mathbf{U}^h) \\
& + \gamma M_{smag}^R(\mathbf{W}^h, \mathbf{U}^h; C_S, h)
\end{aligned} \tag{11}$$

$$M_{smag}^R(\mathbf{W}^h, \mathbf{U}^h; C_S, h) = \int_{\Omega} w_{i,j}^h \underbrace{2 (C_S h)^2 |S^h| S_{ij}^h}_{\nu_t} d\Omega \tag{12}$$

In Equation (12), ν_t is the eddy viscosity, $|S^h|$ is the norm of the strain-rate tensor (i.e., $|S^h| = \sqrt{2\mathbf{S}^h : \mathbf{S}^h} = \sqrt{2S_{ij}^h S_{ij}^h}$), h is the local mesh size, and C_S is the Smagorinsky parameter. The parameter γ is set to be either 0 or 1 in order to control which model is used for the Reynolds stresses. Note that $\gamma = 0$ results in the original RBVMS model and $\gamma = 1$ results in the combined subgrid-scale model. In this study, $\gamma = 1$ is employed. The Smagorinsky parameter is computed dynamically in a local fashion as discussed below.

B. Dynamic Procedure

To dynamically compute the Smagorinsky parameter in a local fashion, we follow the localized version of the variational Germano identity (VGI) developed by Tran *et al.* [10]. In this procedure, Lagrangian averaging along fluid pathtubes is applied to make it robust and which maintains the localized nature of the VGI. The dynamic local procedure and the associated approximations are summarized in this section.

1. Local Variational Germano Identity

The VGI involves comparing the variational form (including the model terms) between different levels of the discretization such that they are nested. In the localized version of the VGI, a set of nested spaces are constructed by using a series of coarser second-level grids along with the primary or original grid. We refer to the primary grid as the h -grid and any grid in the series of second-level grids as the H -level grid. Each H -level grid is chosen such that it is associated with an interior node in the primary grid. This is done such that each H -grid is identical to the h -grid except that the given node k in the h -grid is coarsened or removed resulting in a nested H -level grid for node k , which we refer to as the H_k -grid. Note that each H_k -grid involves local coarsening around a given node k while the remainder of the mesh remains the same. This is demonstrated in 1-D in Figure 1, where Ω^{H_k} is the macro element in the H_k -grid corresponding to node k while Ω^{P_k} is the corresponding patch of elements around node k in the h -grid. Note that $k = 1, 2, \dots, n_{intr}$, where n_{intr} is the number of interior nodes in the h -grid. Therefore, there are n_{intr} grids at the H level, each of which is paired with the primary h -grid. This results in the following spaces for each interior node, $\mathcal{U}^{H_k} \subset \mathcal{U}^h \subset \mathcal{U}$ and $\mathcal{V}^{H_k} \subset \mathcal{V}^h \subset \mathcal{V}$, for the solution and weight functions, respectively.

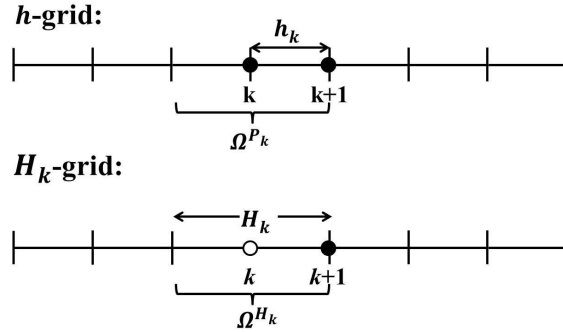


Fig. 1 1-D schematic of the h - and H -level grids for local VGI

The local VGI procedure then uses the H_k -grids with the h -grid to compute the model parameter at every node k in the h -grid. By setting $\mathbf{W}^h = \mathbf{W}^{H_k}$, since $\mathcal{V}^{H_k} \subset \mathcal{V}^h \subset \mathcal{V}$, we get the following (for details see [10]).

$$M_{comb}(\mathbf{W}^{H_k}, \mathbf{U}^h; C_S^k, h_k) - M_{comb}(\mathbf{W}^{H_k}, \mathbf{U}^{H_k}; C_S^k, H_k) = -(B(\mathbf{W}^{H_k}, \mathbf{U}^h) - B(\mathbf{W}^{H_k}, \mathbf{U}^{H_k})) \quad (13)$$

We recognize that determining \mathbf{U}^{H_k} for each interior node k involves a grid-level computation or projection (operations which involve looping over the elements of the H_k -grid). This is prohibitive and therefore, a surrogate is considered. \mathbf{U}^{H_k} is approximated within the macro element using a volume-weighted average of \mathbf{U}^h while outside of the macro element the solution is assumed to be the same between the two grid levels. This assumption further bypasses a grid-level computation. This assumption arises from the requirement on the variational multiscale (VMS) method to provide a localization at the element level and the desire to yield nodal exactness at element corners[14]. This leads to $\mathbf{U}^{H_k} \approx \tilde{\mathbf{U}}^{H_k}|_{\Omega^{H_k}} = \mathbb{A}^{H_k}(\mathbf{U}^h)$, where \mathbb{A}^{H_k} is the local averaging operator defined below.

$$\mathbb{A}^{H_k}(f^h) = \frac{1}{|\Omega^{P_k}|} \int_{\Omega_e^h \in \Omega^{P_k}} f^h d\Omega_e^h \quad (14)$$

where $|\Omega^{P_k}|$ is the volume of the local patch and Ω_e^h indicates an element in the h -grid.

This choice is only feasible when the spatial derivatives exist on the weight function. In addition, instead of using $\tilde{\mathbf{U}}^{H_k}$ to compute \mathbf{S}^{H_k} , \mathbf{S}^{H_k} is also approximated within the macro element as $\tilde{\mathbf{S}}^{H_k}|_{\Omega^{H_k}} \approx \mathbb{A}^{H_k}(\mathbf{S}^h)$. Furthermore, among all of the terms in Equation (13) not involving the unknown model parameter, the non-linear convective term is found to be dominating[10]. We note that this assumption holds exactly in a spectral setting where all the bilinear terms cancel out between the H - and h -level grids due to the L_2 orthogonality of spectral modes[15]. The local VGI simplifies to

$$\begin{aligned}
& -(B_2(\mathbf{W}^{H_k}, \mathbf{U}^h)_{\Omega^{P_k}} - B_2(\mathbf{W}^{H_k}, \tilde{\mathbf{U}}^{H_k})_{\Omega^{H_k}}) \\
& M_{smag}(\mathbf{W}^{H_k}, \mathbf{U}^h; C_S^k, h_k)_{\Omega^{P_k}} - M_{smag}(\mathbf{W}^{H_k}, \tilde{\mathbf{U}}^{H_k}; C_S^k, H_k)_{\Omega^{H_k}}
\end{aligned} \tag{15}$$

Now an appropriate choice for $\mathbf{W}^{H_k} \in \mathcal{V}^{H_k}$ must be made. In a 1D setting, we select $\mathbf{W}^{H_k} = [w_i^{H_k}, 0]^T$ with $w_i^{H_k}$ such that it is linear along a spatial direction within the macro element and is constant or flat outside. Within the macro element, $w_i^{H_k}$ is selected such that

$$w_{i,j}^{H_k} = \frac{1}{|\Omega^{H_k}|} \tag{16}$$

where $|\Omega^{H_k}|$ is the volume of the element. This choice of \mathbf{W}^{H_k} is feasible in a multi-D setting and on an unstructured mesh consisting elements of mixed topology, however, a larger patch must be considered. An extra layer of elements is needed around the macro element to attain a constant value in the outside region. This extra layer acts as a buffer region. This choice is made due to its ease of implementation. For more details see XXX Refs. [10].

2. Local VGI Computation

At this point we drop the subscript k in H_k and P_k and superscript k in C_S^k for brevity and only use it when necessary. The residual of the local VGI is defined as

$$\epsilon_{ij} = L_{ij} - 2(C_S h)^2 M_{ij} \tag{17}$$

where

$$L_{ij} = \left(\left(\frac{1}{|\Omega^{H^h}|}, u_i^h u_j^h \right)_{\Omega^P} - \left(\frac{1}{|\Omega^{H^H}|}, \tilde{u}_i^H \tilde{u}_j^H \right)_{\Omega^H} \right) \tag{18}$$

$$M_{ij} = \left(\left(\frac{1}{|\Omega^{H^h}|}, |S^h| S_{ij}^h \right)_{\Omega^P} - \left(\frac{H}{h} \right)^2 \left(\frac{1}{|\Omega^{H^H}|}, |\tilde{S}^H| \tilde{S}_{ij}^H \right)_{\Omega^H} \right) \tag{19}$$

The least squares method is applied to determine the model parameter as follows

$$(C_S h)^2 = \frac{1}{2} \frac{L_{ij} M_{ij}}{M_{ij} M_{ij}} \tag{20}$$

Since the local VGI procedure often leads to negative values for $(C_S h)^2$, an averaging scheme is employed to avoid this issue. Specifically, Lagrangian averaging is applied[16]. To do so, two additional advection-relaxation scalar equations are solved. These are shown in Equations (21) and (22). The scalars I_{LM} and I_{MM} in these equations are the Lagrangian-averaged counterparts of $L_{ij} M_{ij}$ and $M_{ij} M_{ij}$, respectively.

$$I_{LM,t} + (u_j - u_j^m) I_{LM,j} = \frac{1}{T} (L_{ij} M_{ij} - I_{LM}) \tag{21}$$

$$I_{MM,t} + (u_j - u_j^m) I_{MM,j} = \frac{1}{T} (M_{ij} M_{ij} - I_{MM}) \tag{22}$$

where T is the timescale over which averaging is applied. Additionally, a local volume-weighted averaging is also applied separately to the numerator and denominator of Equation (20) as follows

$$(C_S h)^2 = \frac{1}{2} \frac{\mathbb{A}^H(I_{LM})}{\mathbb{A}^H(I_{MM})} \tag{23}$$

where, as before, \mathbb{A}^H represents a local averaging operator. This is equivalent to averaging over local pathtubes[10, 13] and maintains the utility of the local VGI.

III. Problem Setup and Discretization

A schematic of the problem setup is shown in Figure 2, where U_∞ is the free-stream or mean velocity and α is the angle of attack.

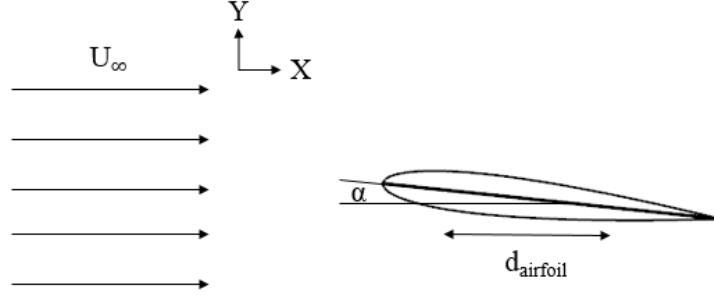


Fig. 2 Schematic of the problem

The airfoil motion is set as follows

$$d_{\text{airfoil}} = A \cos(2\pi ft) = A \cos(2\pi t/T) = A \cos(2\pi \tilde{t}) \quad (24)$$

where A is the amplitude and $T = 1/f$ is the time period of the oscillation. The variable \tilde{t} is the fractional part in the oscillation cycle and is defined as $\tilde{t} = \{t/T\} = t/T - \lfloor t/T \rfloor$ (where $\lfloor \cdot \rfloor$ is the floor function).

The (non-dimensional) relative velocity is expressed as

$$\tilde{U}_{rel} = U_{rel}/U_\infty = 1 - U_{\text{airfoil}}/U_\infty = (1 + \lambda \sin(2\pi \tilde{t})) \quad (25)$$

where λ is the sectional advance ratio. Note that for an advance ratio above 1.0 a negative relative velocity or a reversed flow condition is attained. Under this condition the relative flow is from the (geometric) trailing edge to the leading edge of the airfoil.

At $\tilde{t}=0$, with $\phi=0^\circ$ or $\psi=0^\circ$ (where, ϕ is the phase in the oscillation cycle and ψ is the azimuthal position of the blade), the relative velocity is the free-stream velocity (i.e., U_∞). The same holds at $\tilde{t}=0.5$ or $\phi=180^\circ$. At $\tilde{t}=0.25$ or $\phi=90^\circ$, the airfoil is at the maximum relative velocity and at $\tilde{t}=0.75$ or $\phi=270^\circ$ is at the minimum relative velocity. Advancing phase is defined between $\tilde{t}=0$ or $\phi=0^\circ$ and $\tilde{t}=0.5$ or $\phi=180^\circ$ while retreating phase is between $\tilde{t}=0.5$ or $\phi=180^\circ$ and $\tilde{t}=1.0$ or $\phi=360^\circ$ (or back to $\phi=0^\circ$).

The free-stream or mean Reynolds number is defined as $Re = U_\infty C/\nu$, where C is the chord. The reduced frequency is defined as $k = \pi f C/U_\infty$ while the amplitude is related as $A = \frac{\lambda C}{2k}$.

In the current study, the reduced frequency is held fixed at $k=0.133$ while three Reynolds numbers of $Re=40,000$, $200,000$ and $1,000,000$ are considered together with two advance ratios of $\lambda=1.0$ and 1.2 , i.e., six cases are considered in total. The angle of attack of the airfoil is set to 6° . Note that we considered the Reynolds number of $Re=40,000$ in previous study [17] that was selected in accordance with the experiments conducted in [2] where the airfoil was placed in a constant flow and oscillated in the streamwise direction. The six cases are summarized in Table 1.

Table 1 Summary of cases

Airfoil	α	k	λ	Re
NACA 0012	6°	0.133	{1.0, 1.2}	{40,000, 200,000, 1,000,000}

The computational domain is set to be $100C \times 50C \times 0.2C$. At the inlet, a constant free-stream velocity is applied (note that the airfoil is moved sinusoidally in the streamwise direction). No-slip condition is prescribed on the airfoil surface. The top and bottom surfaces are set as slip walls. Side surfaces in the spanwise direction (i.e., front and back surfaces) are imposed to be periodic. A natural pressure condition is used at the outlet. A second-order implicit time integration scheme, e.g., see [10], is employed with about 1,440 steps in an oscillation cycle.

An unstructured hybrid/boundary layer mesh is used. The mesh is comprised of hex and wedge elements which is generated by applying an extrusion in the spanwise direction. Refinement zones are placed around the airfoil to resolve the flow structures of interest, see Figure 3 (where three refinement zones are noted). In the finest refinement zone (Z1), mesh size is set to be $C/256$. In the subsequent two zones (Z2 and Z3), it is set to be $C/128$ and $C/64$, respectively. In the spanwise direction, 50 extruded elements are used. A layered and graded mesh (with geometric growth) is used around the airfoil surface, see Figure 4. The first layer height is set to be $O(10^{-5}C)$ such that it is below 1 in wall units. Similarly, mesh spacing on the airfoil surface in the streamwise and spanwise directions is set to be below 80 and 50 in wall units, respectively. Overall the mesh contains about 6.2 million nodes and 10.8 million elements.

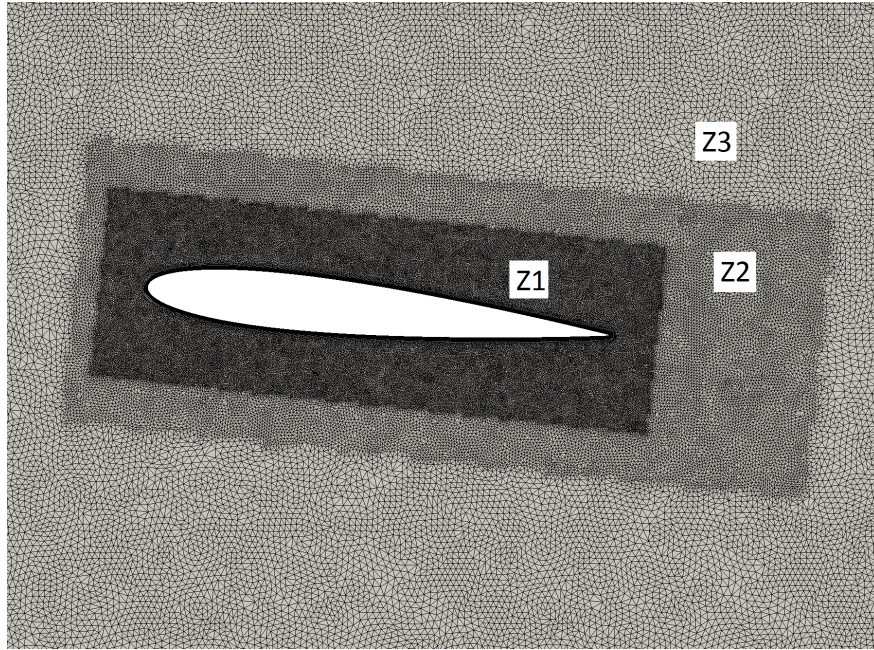


Fig. 3 Mesh around the airfoil with refinement zones

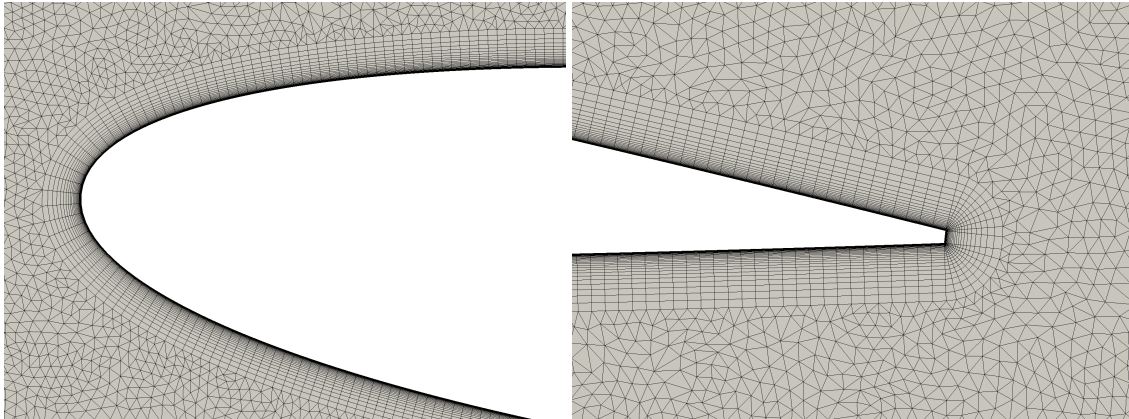


Fig. 4 Layered and graded mesh around the leading edge and trailing edge of the airfoil

IV. Results and Discussion

In this paper, we present LES predictions for the force response, spanwise vorticity and leading edge vortex (LEV) evolution for all six cases. For each case, simulations are carried over 5 oscillation cycles and a limit cycle behavior is

observed after the first cycle. Therefore, the presented data is collected over the last 4 cycles, where phase averaging is employed based on the oscillation frequency. In addition, averaging is also applied in the spanwise direction.

A. Force Response

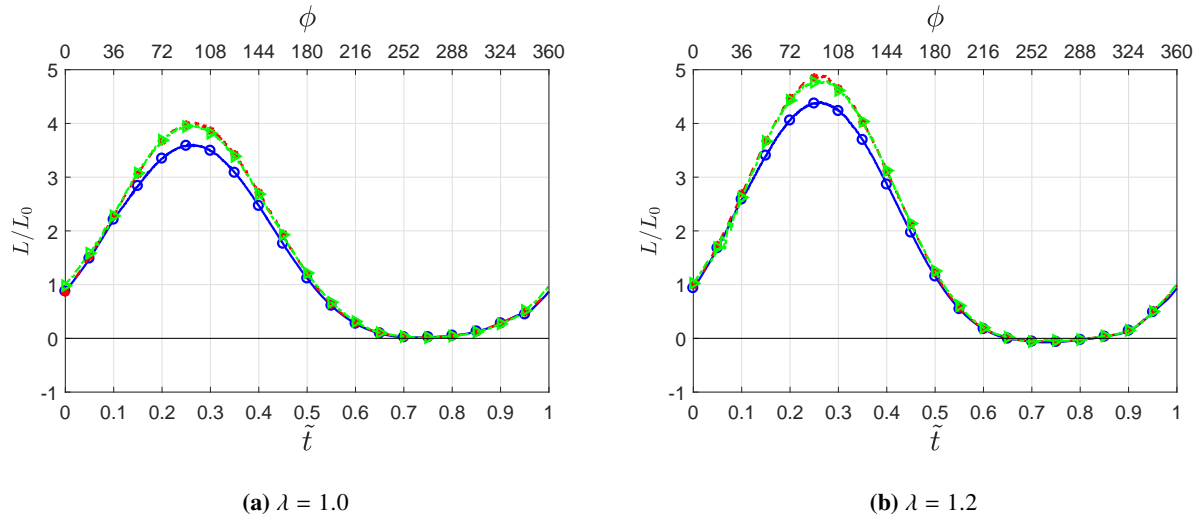


Fig. 5 Normalized lift force for $Re=40,000$ (green line with open triangles), $200,000$ (red line with closed circles) and $1,000,000$ (blue line with open circles) at $\lambda=1.0$ and 1.2

Lift force is shown in Figure 5. Lift is normalized by its static counterpart, i.e., L_0 is the average or steady lift for the static airfoil at mean Reynolds number. This normalization was used in our previous study with $Re=40,000$ [17] to compare against the experimental data of [2], where a good agreement was shown between the experimental and simulation data. As noted earlier, data is phase averaged over 4 cycles.

Overall, the lift force follows a similar qualitative trend for all the cases. Maximum lift is achieved at $\tilde{t} = 0.25$, which is expected as the airfoil achieves maximum relative velocity at that point. After $\tilde{t} = 0.25$, the lift starts decreasing as the airfoil begins to decelerate and enters the retreating phase. The lift keeps decreasing till about $\tilde{t} = 0.65$ and plateaus or reaches a value close to zero during the middle of the retreating phase (i.e., around $\tilde{t} = 0.75$ when the airfoil is at its minimum relative velocity). We note that for both advance ratios of $\lambda=1.0$ and 1.2 a zero relative velocity is attained and for the higher advance ratio of $\lambda=1.2$ the relative velocity also becomes negative. Lift starts to recover after $\tilde{t} = 0.75$ as the airfoil starts accelerating again. For each advance ratio, the normalized lift during the advancing phase for $Re=1,000,000$ is smaller compared to the other two Reynolds numbers, see Figure 5a or Figure 5b. The normalized lift is very similar between $Re=40,000$ and $200,000$ cases. The peak normalized lift is about 9% lower for the highest Reynolds number case as compared to the lower Reynolds number cases for each advance ratio. On the other hand, for a given Reynolds number the normalized lift is higher for the higher advance ratio, which is expected due to higher dynamic pressure in an instantaneous sense. The peak normalized lift is about 21% higher for the higher advance ratio case as compared to the lower advance ratio case for each Reynolds number, which is the difference in the peak dynamic pressure between the two advance ratios.

B. Flowfields

In this section, we present spanwise vorticity over the cycle at 8 different phases of $\phi = 195^\circ, 225^\circ, 240^\circ, 255^\circ, 270^\circ, 315^\circ, 330^\circ$ and 345° , which are all in the retreating phase of the cycle. We focus our attention on the LEV which is the dominant flow feature. It forms and advects during the retreating phase while in the advancing phase the flow remains attached. As noted earlier, data is phase averaged over 4 cycles. In addition, averaging is also applied in the spanwise direction.

1. $\lambda = 1.0$

Figure 6 shows the spanwise vorticity for the lower advance ratio of $\lambda=1.0$. 8 different phases over the retreating phase of the cycle are shown and the range is selected to be $[-10,10]\times U_\infty/C$. At $\phi=195^\circ$, the flow over the airfoil is mostly attached, however, the boundary layer is relatively thick as the airfoil is decelerating, see Figures 6a, 6b and 6c. As expected, the boundary layer is much thicker for the lowest Reynolds number of $Re=40,000$ as compared to the other two higher Reynolds number.

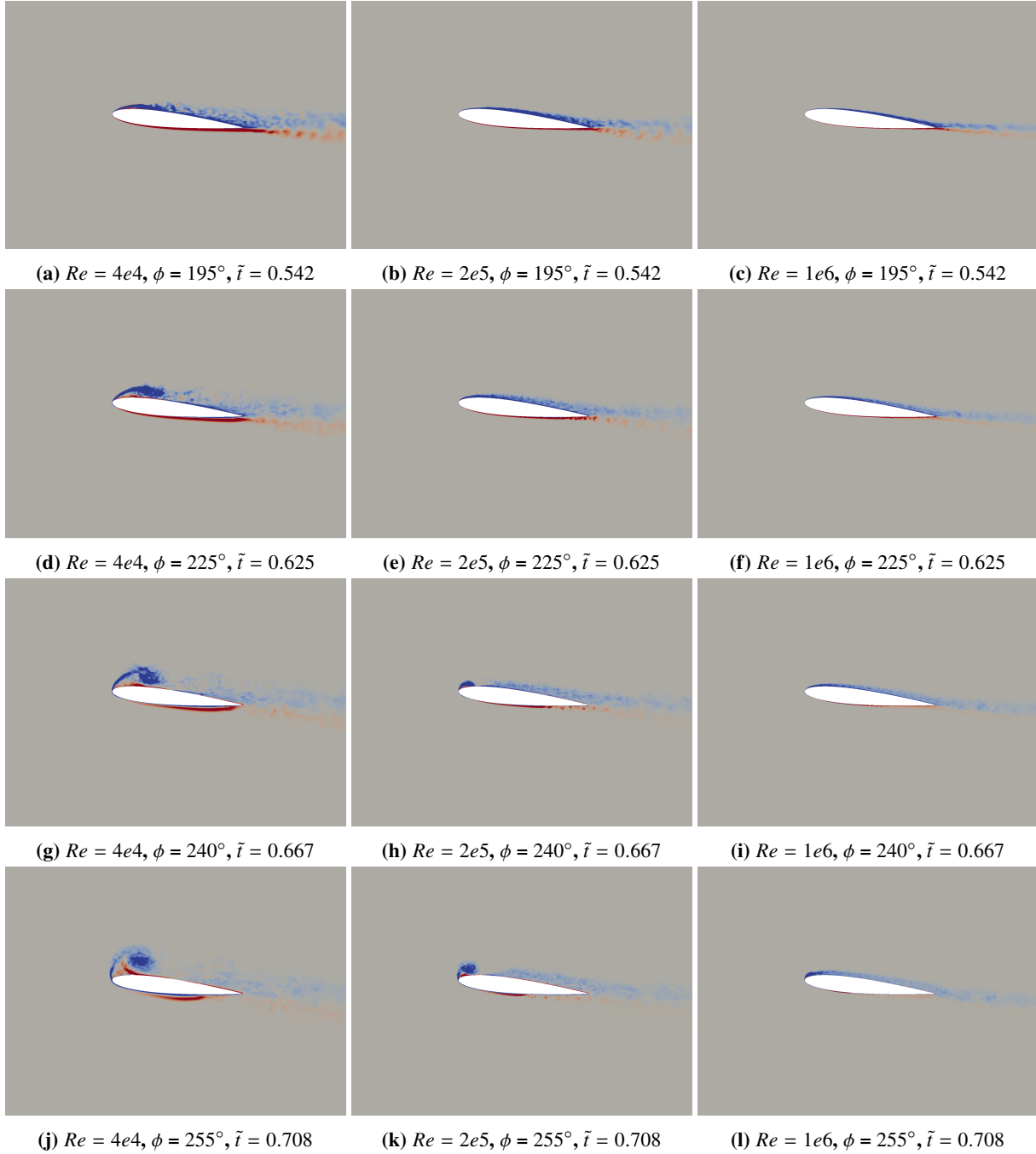


Fig. 6 Spanwise vorticity at 8 different phases for $Re=40,000$ (left column), $200,000$ (middle column) and $1,000,000$ (right column) at $\lambda = 1.0$

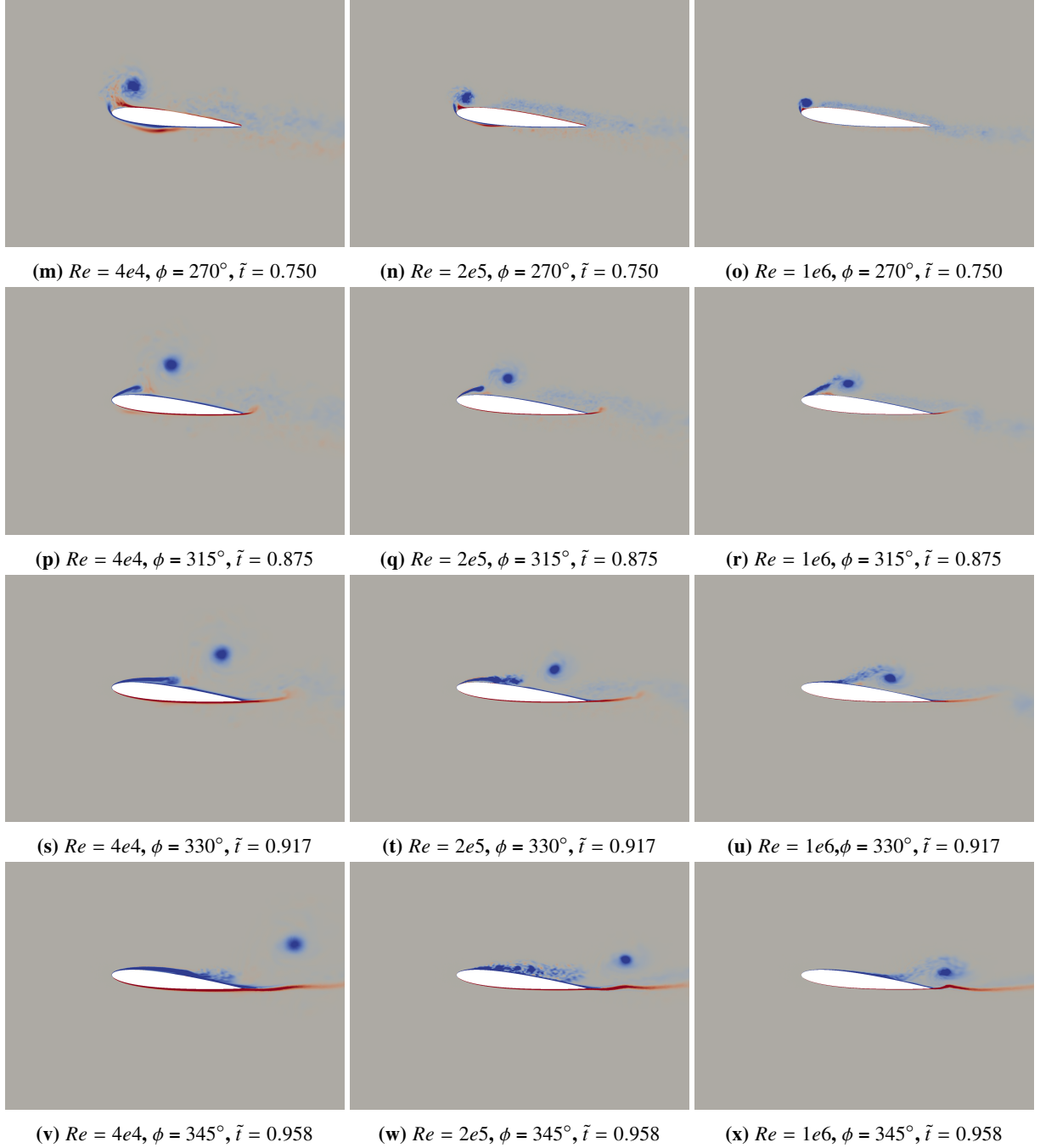


Fig. 6 Spanwise vorticity at 8 different phases for $Re=40,000$ (left column), $200,000$ (middle column) and $1,000,000$ (right column) at $\lambda = 1.0$

At $\phi=225^\circ$, the flow is separated near the leading edge for the lowest Reynolds number of $Re=40,000$ and the separated shear layer rolls up into an LEV, see Figure 6d. For the other two higher Reynolds number, the flow remains attached. Similarly, at $Re=200,000$ the separated shear layer rolls up into a small LEV at $\phi=240^\circ$ (see Figure 6h) while for $Re=1,000,000$ this occurs at $\phi=270^\circ$ (see Figure 6o). As the Reynolds number increases the LEV is formed later in the cycle. In summary, as the airfoil retreats vorticity accumulates around the airfoil and separated shear layer rolls up into a distinct vortex near the leading edge (i.e., an LEV) over the suction or upper side of the airfoil.

In subsequent phases, LEV is ejected into the outer flow and advects. The flow on the suction or upper side reattaches as the leading edge vortex passes over the airfoil. Flow also separates and reattaches on the pressure or lower side, e.g.,

see marginal flow separation at the trailing edge on the lower side in Figures 6d and 6g.

It is important to note the differences in LEV evolution with different Reynolds number even though the overall trend of the LEV evolution is similar between different Reynolds number. As already noted, the phase at which the LEV is formed changes with Reynolds number. Further, the size and vertical position of the LEV also changes significantly with Reynolds number. This aspect is discussed in Section IV.C.

2. $\lambda = 1.2$

Figure 7 shows the spanwise vorticity for the higher advance ratio of $\lambda=1.2$. Again, 8 different phases over the retreating phase of the cycle are shown and the range is selected to be $[-10,10] \times U_\infty/C$. As in the $\lambda = 1.0$ case, at $\phi=195^\circ$ the flow over the airfoil is mostly attached in the $\lambda = 1.2$ case. As before, the boundary layer is much thicker for the lowest Reynolds number of $Re=40,000$ as compared to the other two higher Reynolds number.

At $\phi=225^\circ$, the flow is fully separated for the lowest Reynolds number of $Re=40,000$ and the separated shear layer is rolled up into an LEV, see Figure 7d. Similarly, at $Re=200,000$ a small LEV is seen at $\phi=225^\circ$ (see Figure 7e) while for $Re=1,000,000$ LEV is observed at $\phi=240^\circ$ (see Figure 7i). As before, as the Reynolds number increases the LEV is formed later in the cycle. On the other hand, as the advance ratio increases it is formed earlier in the cycle (for a given Reynolds number). For example, in Figure 6o and Figure 7i for $Re=1,000,000$, the LEV is formed at an earlier phase for $\lambda = 1.2$ as compared to $\lambda = 1.0$. As before, as the airfoil retreats vorticity accumulates and shear layer rolls up into a distinct LEV over the suction or upper side of the airfoil.

In subsequent phases, LEV is ejected into the outer flow and advects while the flow reattaches. However, at the higher advance ratio of $\lambda=1.2$ the LEV initially moves to the left past the (geometric) leading edge of the airfoil. This is because at $\lambda=1.2$ the relative flow velocity becomes negative and a reversed flow condition is reached. Again, it is important to note the differences in LEV evolution with different Reynolds number for the advance ratio of $\lambda = 1.2$. As already noted, the size, position and phase of formation of LEV changes significantly with Reynolds number. This aspect is discussed in Section IV.C.

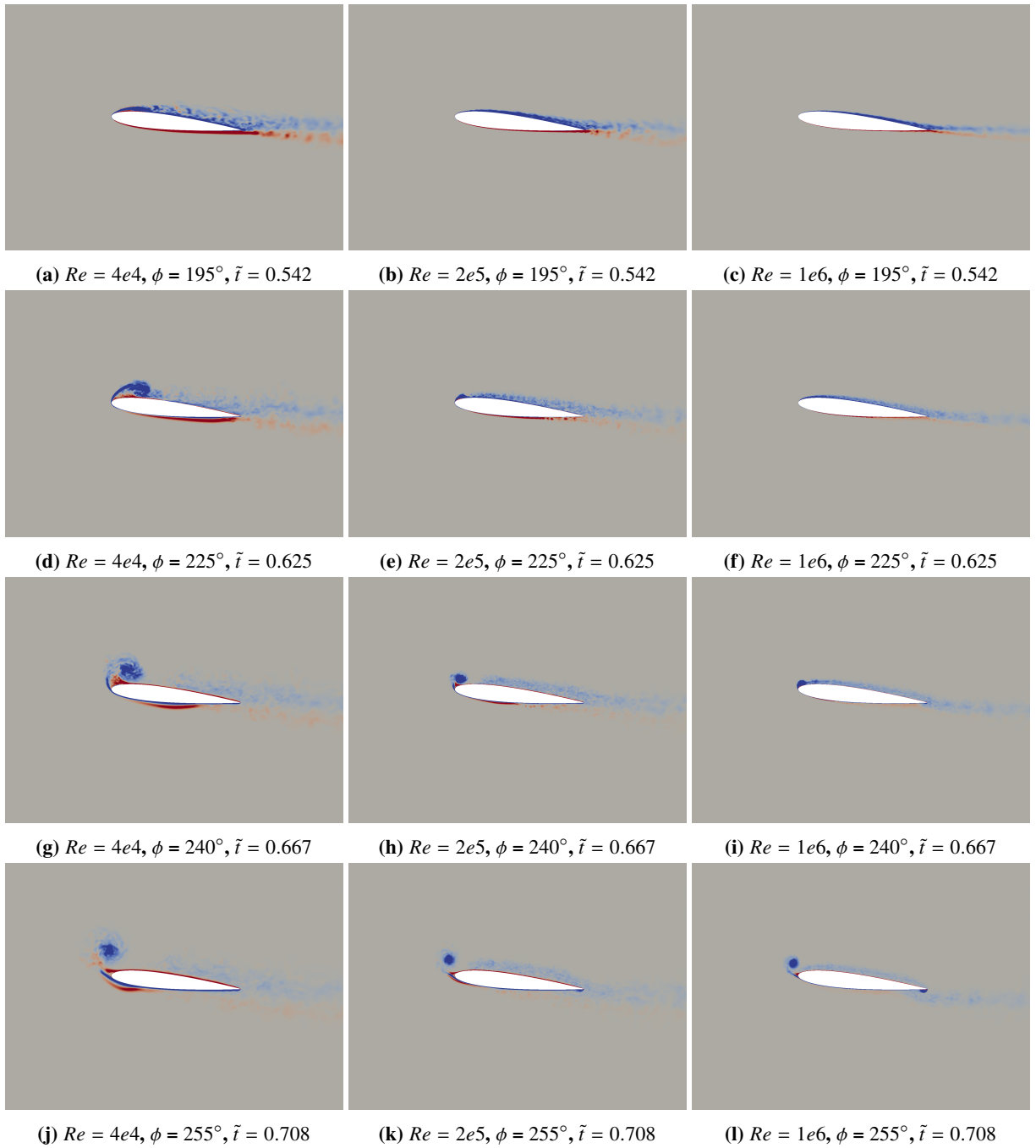


Fig. 7 Spanwise vorticity at 8 different phases for $Re=40,000$ (left column), $200,000$ (middle column) and $1,000,000$ (right column) at $\lambda = 1.2$

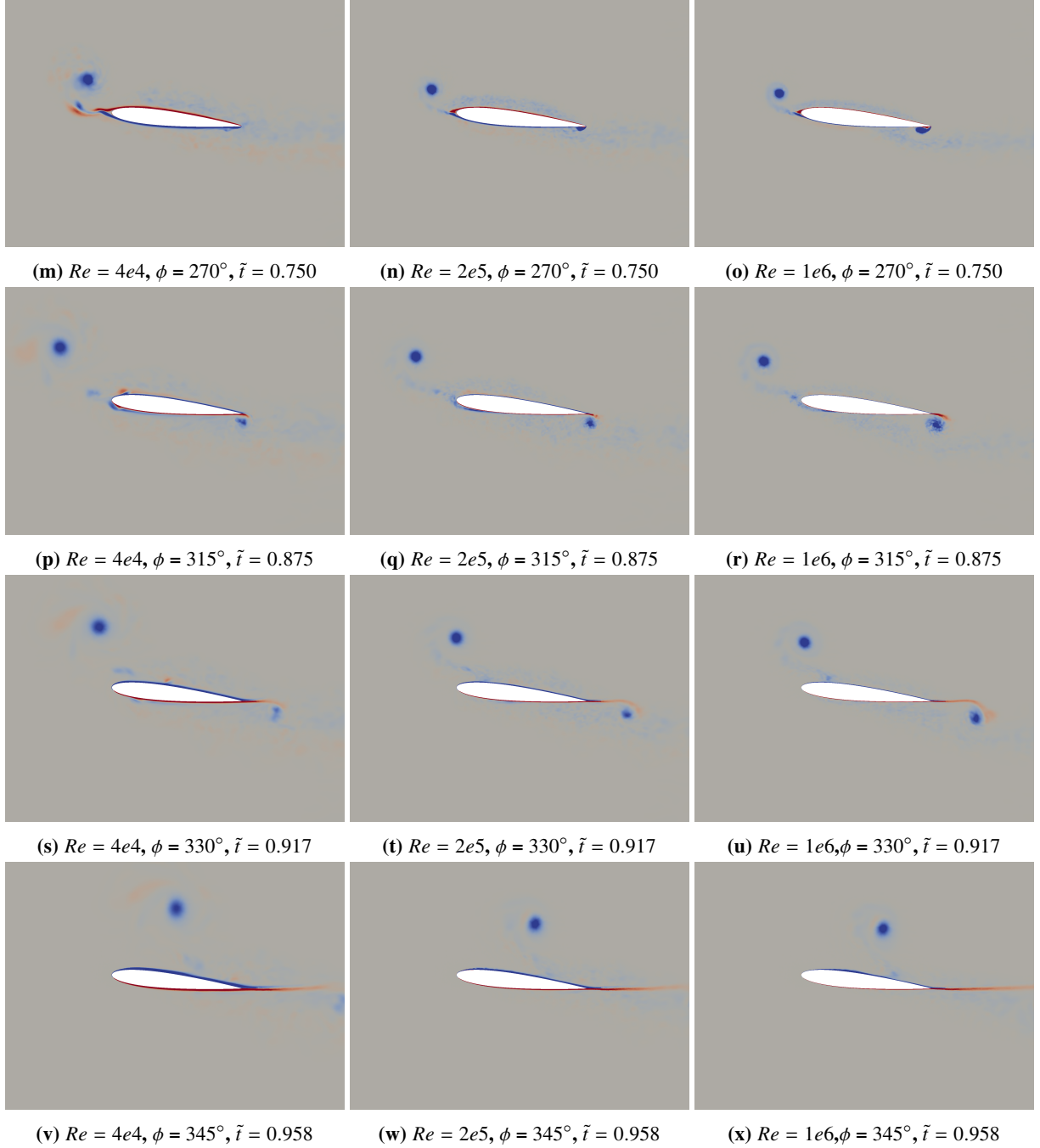


Fig. 7 Spanwise vorticity at 8 different phases for $Re=40,000$ (left column), $200,000$ (middle column) and $1,000,000$ (right column) at $\lambda = 1.2$

C. LEV Evolution

In this section, we quantify the evolution of the LEV based on its size and position. In order to do so, for each case at first the phase of formation of the LEV is detected and in subsequent phases the LEV is tracked. Pressure and velocity data is analyzed to detect the formation of the LEV. In the retreating portion of the cycle, location with minimum pressure is determined starting at $\phi = 180^\circ$. The first phase at which the minimum pressure location is off the airfoil surface (i.e., away from the airfoil and into the flow) is tagged to be a potential phase for LEV formation. At this potential phase, velocity profile is obtained over multiple lines passing through the minimum pressure location.

These lines are taken at an equispaced interval along the azimuthal direction in the plane of the airfoil (note that the data is averaged in the spanwise direction). Along these lines, at first a relative velocity is computed with respect to the velocity at the minimum pressure location. Subsequently, normal component of the relative velocity is obtained (i.e., normal to each line), which is the azimuthal or tangential component in the polar coordinate system centered around the minimum pressure location. The azimuthal component (of the relative velocity) is analyzed against the velocity profile of a Rankine vortex. In the case when azimuthal component (along the line) fits a linear variation for a certain distance about the minimum pressure location, an LEV is successfully detected. The first phase during the retreating portion of the cycle, when an LEV is successfully detected, is tagged to be the phase of formation of the LEV. The minimum pressure location is set as the initial LEV position. Further, the extent (along the line) of the linear variation of the azimuthal component of the relative velocity is set as the diameter, or twice the radius, of the vortex core. This radius defines the central core of the Rankine vortex. It is noteworthy that azimuthal component of the relative velocity along several lines at multiple phases were visually analyzed for different cases and found to fit the Rankine vortex model fairly well.

Figure 8 presents the size or core radius (r_c) of the LEV for all six cases. We note that in simulations the data was recorded at every $\Delta\phi = 15^\circ$ starting at $\phi=15^\circ$. For each case the LEV is formed at about $\tilde{t} = 0.6$ or later. The LEV size is higher for the lowest Reynolds number of $Re=40,000$ for both advance ratios of $\lambda=1.0$ and 1.2 . This is expected since the boundary layer is thicker for $Re=40,000$ and the resulting separated shear layer rolls up into a larger LEV. The LEV size is very similar for the other two higher Reynolds numbers at $\lambda=1.0$ and 1.2 . In the $\lambda=1.0$ case, the LEV increases in size till about $\tilde{t} = 0.75$ to 0.8 and subsequently seem to plateau or increase in size relatively slowly. Towards the end of the cycle, the LEV size is about 8% of the chord for $Re=40,000$ at $\lambda=1.0$, and about 6% for $Re=200,000$ and $1,000,000$ at $\lambda=1.0$. In the $\lambda=1.2$ case, the LEV increases in size throughout the cycle and towards the end of the cycle reaches about a similar size as the $\lambda=1.0$ case for each Reynolds number.

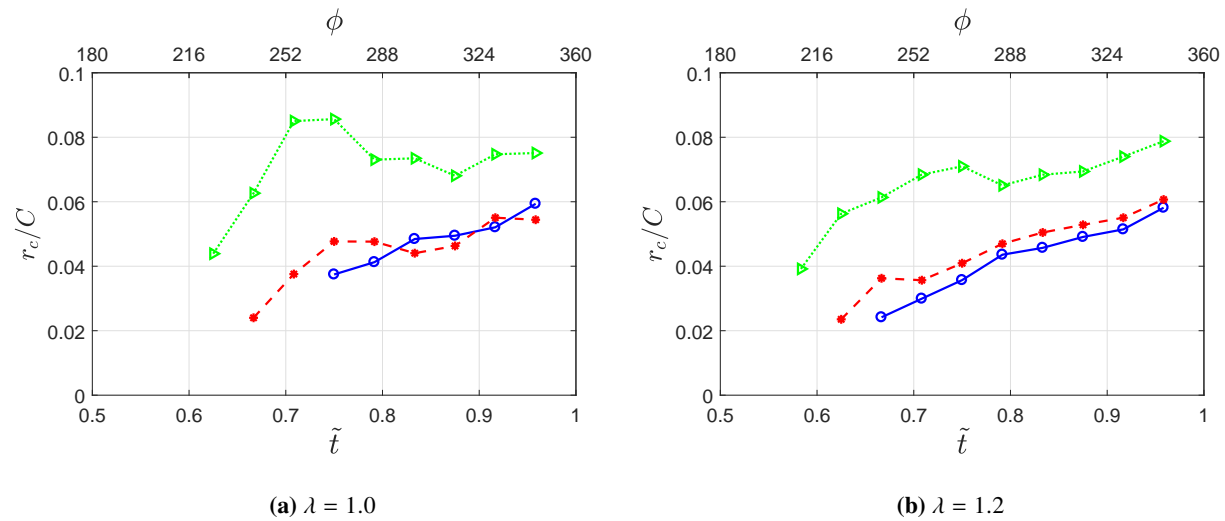


Fig. 8 LEV size for $Re=40,000$ (green line with open triangles), $200,000$ (red line with closed circles) and $1,000,000$ (blue line with open circles) at $\lambda=1.0$ and 1.2

LEV position with respect to the leading edge of the airfoil is presented in Figure 9. In the $\lambda = 1.0$ case, the initial position of the LEV (i.e., position at formation) gets closer to the leading edge as the Reynolds number is increased. Further, LEV remains closest to the airfoil over the cycle for the highest Reynolds number of $Re=1,000,000$ (i.e., note the vertical position of the LEV). On the other hand, LEV initially moves to the left (towards the geometric leading edge) from its initial position for the lowest Reynolds number of $Re=40,000$. In the $\lambda = 1.2$ case also, similar trends are observed. However, at the higher advance ratio the LEV initially moves to the left past the geometric leading edge for each Reynolds number. This is expected since the relative flow velocity becomes negative (or a reversed flow condition is obtained) at $\lambda = 1.2$.

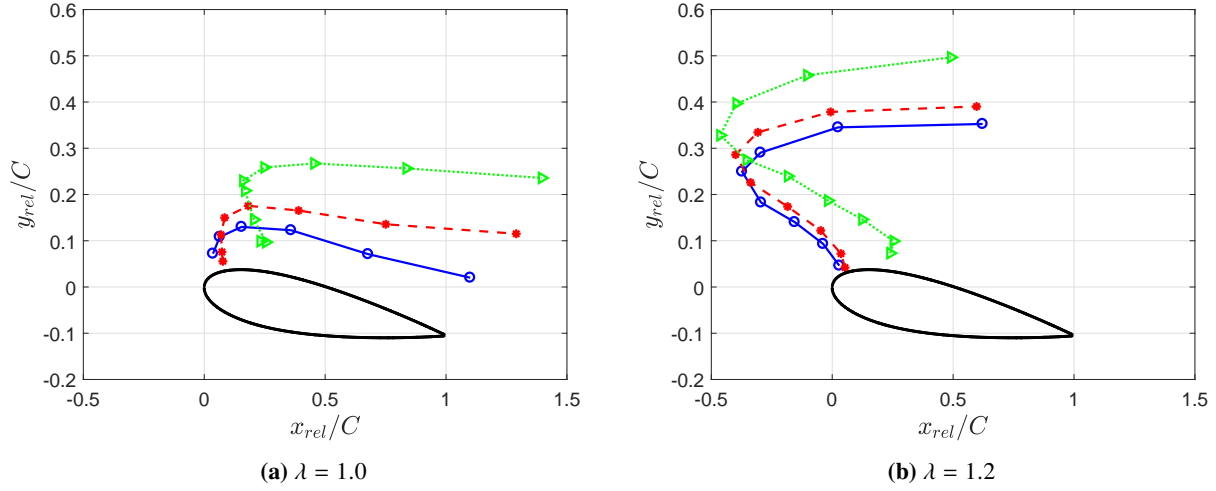


Fig. 9 LEV position (with respect to the leading edge of the airfoil) for $Re=40,000$ (green line with open triangles), $200,000$ (red line with closed circles) and $1,000,000$ (blue line with open circles) at $\lambda=1.0$ and 1.2

In Figure 10, the horizontal displacement of the LEV with respect to the ground is presented. The displacement is taken about the initial position when the LEV is formed, i.e., the displacement is zero at the initial position. Again, as the Reynolds number increases the LEV is formed later in the cycle (for a given advance ratio) while as the advance ratio increases it is formed earlier in the cycle (for a given Reynolds number).

An important aspect to note in Figure 10 is that the horizontal displacement of the LEV follows a straight line for each case and is parallel among all cases. The slope of the horizontal displacement in each case is remarkably close to the free-stream velocity, i.e., the LEV is advected in the horizontal direction at the free-stream velocity.

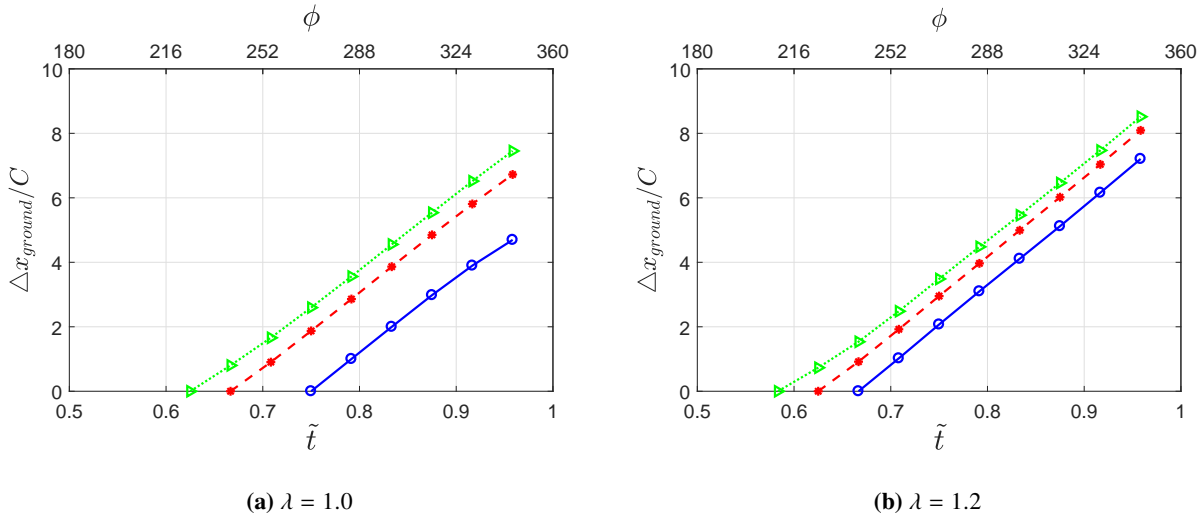


Fig. 10 LEV displacement (in the horizontal direction) for $Re=40,000$ (green line with open triangles), $200,000$ (red line with closed circles) and $1,000,000$ (blue line with open circles) at $\lambda=1.0$ and 1.2

V. Closing Remarks

LES was performed for flow over a surging NACA 0012 airfoil with large streamwise oscillations or advance ratios at high Reynolds numbers. The NACA 0012 airfoil was subjected to sinusoidal streamwise oscillations. A fixed frequency, angle of attack and a steady free-stream flow was considered. Three Reynolds numbers of $Re=40,000$, $200,000$ and $1,000,000$ were considered together with two advance ratios of $\lambda=1.0$ and 1.2 , i.e., six cases were considered in total.

Overall a similar trend was observed in the lift force among all cases. The peak normalized lift for the highest Reynolds number case was about 9% lower as compared to the lower Reynolds number cases for each advance ratio, while it was about 21% higher for the higher advance ratio case as compared to the lower advance ratio case for each Reynolds number. Flow field also revealed a similar behavior among all cases with prominent features of flow separation near the (geometric) leading edge during the beginning of the retreating phase and formation of a dominant leading edge vortex. As the Reynolds number increased the LEV formed at a later point in the cycle while as the advance ratio was decreased it formed earlier in the cycle. LEV was quantified based on its size and position. The central core of the LEV was found to fit the Rankine vortex model. Larger LEV was obtained for the lowest Reynolds number while the vertical position was found to be closest to the airfoil for the highest Reynolds number. Further, LEV initially moved to the left past the geometric leading edge at the higher advance ratio for each Reynolds number. In addition, the horizontal velocity of the LEV (with respect to ground) was found to be remarkably close to the free-stream velocity.

References

- [1] Greenblatt, D., Mueller-Vahl, H., Strangfeld, C., Ol, M. V., and Granlund, K. O., "High advance-ratio airfoil streamwise oscillations: wind tunnel vs. water tunnel," *54th AIAA Aerospace Sciences Meeting*, 2016. AIAA Paper 2016-1356.
- [2] Granlund, K. O., Ol, M. V., and Jones, A. R., "Streamwise oscillation of airfoils into reverse flow," *AIAA Journal*, 2016, pp. 1–9.
- [3] Visbal, M. R., "Analysis of the onset of dynamic stall using high-fidelity large-eddy simulations," *52nd Aerospace Sciences Meeting*, 2014. AIAA Paper 2016-0591.
- [4] Gross, A., and Wen, G., "Numerical investigation of helicopter blade section undergoing time-periodic motions," *8th AIAA Flow Control Conference*, 2016. AIAA Paper 2016-4244.
- [5] Stangfeld, C., Rumsey, C. L., Mueller-Vahl, H., Greenblatt, D., Nayeri, C., and Paschereit, C. O., "Unsteady thick airfoil aerodynamics: experiments, computation, and theory," *45th AIAA Fluid Dynamics Conference*, 2015, p. 3071.
- [6] Hodara, J., Lind, A. H., Jones, A. R., and Smith, M. J., "Collaborative investigation of the aerodynamic behavior of airfoils in reverse flow," *Journal of the American Helicopter Society*, Vol. 61, No. 3, 2016, pp. 1–15.
- [7] Norman, T. R., Shinoda, P., Peterson, R. L., and Datta, A., "Full-scale wind tunnel test of the UH-60A airloads rotor," *American Helicopter Society 67th Annual Forum*, 2011.
- [8] Chaderjian, N. M., and Ahmad, J. U., "Detached eddy simulation of the UH-60 Rotor wake using adaptive mesh refinement," 2012.
- [9] Potsdam, M., Datta, A., and Jayaraman, B., "Computational investigation and fundamental understanding of a slowed UH-60A rotor at high advance ratios," *Journal of the American Helicopter Society*, Vol. 61, No. 2, 2016, pp. 1–17.
- [10] Tran, S., and Sahni, O., "Finite element based large eddy simulation using a combination of the variational multiscale method and the dynamic Smagorinsky model," *Journal of Turbulence*, Vol. 18, 2017, pp. 391–417.
- [11] Cummings, R., Tran, S., and Sahni, O., "Finite element based large eddy simulation of a flow over an oscillating cylinder," *Proc. 8th International Colloquium on Bluff Body Aerodynamics and Applications*, 2016.
- [12] Wang, Z., and Oberai, A. A., "A mixed large eddy simulation model based on the residual-based variational multiscale formulation," *Physics of Fluids*, Vol. 22, No. 7, 2010, p. 075107.
- [13] Tran, S., and Sahni, O., "Large Eddy Simulation based on the Residual-based Variational Multiscale Method and Lagrangian Dynamic Smagorinsky Model," *54th AIAA Aerospace Sciences Meeting*, 2016, p. 0341.
- [14] Hughes, T. J., and Sangalli, G., "Variational multiscale analysis: the fine-scale Green's function, projection, optimization, localization, and stabilized methods," *SIAM Journal on Numerical Analysis*, Vol. 45, No. 2, 2007, pp. 539–557.
- [15] Oberai, A., and Wanderer, J., "Variational formulation of the Germano identity for the Navier-Stokes equations," *Journal of Turbulence*, , No. 6, 2005, p. N7.
- [16] Meneveau, C., Lund, T. S., and Cabot, W. H., "A Lagrangian dynamic subgrid-scale model of turbulence," *Journal of Fluid Mechanics*, Vol. 319, 1996, pp. 353–385.
- [17] Kocher, A., Cummings, R., Tran, S., and Sahni, O., "Large Eddy Simulation of Surging Airfoils with Moderate to Large Streamwise Oscillations," *AIAA Paper 2017-1006*, 2017.